Artificial nociceptor based on TiO$_2$ nanosheet memristor

Jinling Lan[1†], Gang Cao[1], Jingjuan Wang[1] and Xiaobing Yan[1,2†*]

ABSTRACT   With the development of technology, the learning and memory functions of artificial memristor synapses are necessary for realizing artificial neural networks and neural neuromorphic computing. Owing to their high scalability performance, nanosheet materials have been widely employed in cellular-level learning, but the behaviors of nociceptor based on nanosheet materials have rarely been studied. Here, we present a memristor with an Al/TiO$_2$/Pt structure. After electroforming, the memristor device showed a gradual conductance regulation and could simulate synaptic functions such as the potentiation and depression of synaptic weights. We also designed a new scheme that verifies the pain sensitization, desensitization, allodynia, and hyperalgesia behaviors of real nociceptors in the fabricated memristor. Memristors with these behaviors can significantly improve the quality of intelligent electronic devices. Data fitting showed that the high resistance and low resistance states were consistent with the hopping conduction mechanism. This work promises the application of TiO$_2$-based devices in next-generation neuromorphological systems.

Keywords: nanosheets, nociceptor, memristors, artificial synapses, sensitization

INTRODUCTION

In-depth studies of intelligent electronic equipment have revealed the disadvantages of traditional Von Neumann architecture in data processing, power consumption, and other areas. The separation of storage and computation in traditional systems, which has hindered the development of neuromorphological research [1,2], is expected to be resolved by memristors. As a burgeoning technology, memristors can equip neuromorphological systems with excellent data-handling capacity, low power consumption, high density, and convenient configuration; moreover, they are similar to biological synapses [3–6]. In previous studies, the memristor functional layer is composed of oxide materials, which impose challenges such as reducing the size of the device [7–12]. Recently, TiO$_2$ films have demonstrated good electrical properties as well as excellent thermal and chemical stability; moreover, colloidal suspensions of TiO$_2$ can be manufactured over large areas [13]. However, memristors based on oxide nanosheets are currently immature, and their underlying physical mechanism has not yet been clarified. In this work, memristor devices are fabricated from colloidal suspensions of TiO$_2$.

The applications of memristor have gradually diversified into various bionic devices. One research direction is humanoid robots that imitate the human sensory system [14,15]. Pain is an unpleasant bodily response to a harmful stimulation. More specifically, strong noxious stimulations activate the nociceptors in the body, which transmit pain information to the central nervous system [16]. Accordingly, nociceptors are among the most important receptor types. In the present study, a nociceptor is artificially represented by a memristor. After a strong stimulation, the artificial nociceptor is damaged and shows sensitive behavior, followed by desensitization behavior with the increase of stimulus interval. These behaviors are described in detail later.

In this work, TiO$_2$ films were fabricated using a low-cost method based on simple spin coating. Unlike other preparation methods such as physical-vapor, chemical-vapor, and atomic-layer depositions, our preparation involves no complex experimental steps. The device shows

[1] Key Laboratory of Brain-Like Neuromorphic Devices and Systems of Hebei Province, College of Electron and Information Engineering, Hebei University, Baoding 071002, China
[2] Department of Materials Science and Engineering, National University of Singapore, Singapore 117576, Singapore
[†] These authors contributed equally to this work.
[*] Corresponding author (email: yanxiaobing@ime.ac.cn)

basic memristor characteristics under direct voltage, and the resistance of the device can be modulated by an external stimulus (voltage pulses). Besides achieving some basic synaptic plasticity, the devices exhibit nociceptor-like responses that depend on the intensity, duration, and frequency of the external stimuli [17]. In previous reports of memristor-based artificial nociceptors, verification was performed using a complex and cumbersome process [18]. Here, we verify the nociceptor behavior using a new and facile principle. Similar to the biological behavior, the response sensitivity of our device increases with increasing strength of the stimulus and decreases with increasing stimulation interval (the latter behavior is synonymous with desensitization). Our work demonstrates the potential of TiO_2 in bionic research and will encourage the exploration of memristor-based complex learning and memory functions.

EXPERIMENTAL SECTION

Preparation of TiO_2 nanosheets
We first prepared layered potassium-lithium-titanate ($K_{0.8}[Ti_{1.73}Li_{0.27}]O_4$) using a high-temperature solid-phase growth method [19]. The mixture containing TiO_2, K_2CO_3, and Li_2CO_3 were placed in a Pt crucible and reacted at 1173 K for 20 h. The molar ratio of the mixture was 10.4:2.4:0.8. The titanium microcrystals of $K_{0.8}[Ti_{1.73}Li_{0.27}]O_4$ were leached in hydrochloric acid and recycled and converted into proton form. During the leaching process, the crystals were immersed in 0.5 mol L^{-3} hydrochloric acid solution at room temperature for two days. Then, the hydrochloric acid solution was replaced with a fresh hydrochloric acid solution. The protonated product $H_{1.07}Ti_{1.73}O_4$ was filtered, collected, washed, and air-dried. To produce the single-layer titanium dioxide dispersion, the protonated titanate polycrystals were dipped into a tetramethyl ammonium hydroxide solution (($CH_3)_4NOH$, TMAOH) at a concentration equivalent to 1:1 for the exchangeable protons in the initial titanate. The solid-soluble ratio was 4 g L^{-1}.

Fabrication of the $Al/TiO_2/Pt$ device
The memristor was fabricated *via* physical adsorption and magnetron sputtering. First, the colloidal suspension of TiO_2 was coated on cleaned Pt and dried in the air. After this operation was repeated five times, Al layer with a thickness of 60 nm was deposited on the sample *via* radio frequency (RF) magnetron sputtering (at an RF power of 10 W at 3 Pa in an Ar atmosphere of 25 SCCM). Fig. S1 shows a cross-sectional view of the device.

Characterization
The current-voltage (*I-V*) characteristics of the fabricated memristor were measured at room temperature using a Keithley 2400 source meter. The pulse sequences were generated using an Agilent 33250A signal generator and the output waveform was collected by an LeCroy WaveRunner 62Xi oscilloscope.

RESULTS AND DISCUSSION
Fig. 1a, b show an atomic force microscopy (AFM) image and a transmission electron microscopy (TEM) image of the TiO_2 nanosheets, respectively. The $Al/TiO_2/Pt$ memristive devices exhibit typical bipolar-type switching characteristics (Fig. 1c; the inset shows the structure of the device). Before the resistance switching was stabilized, the device was electroformed under a high negative bias, causing soft breakdown of the materials and producing many vacancy defects (Fig. S2) [20–22]. Partial positive and negative *I–V* curves of the memristor are shown in Fig. S3. The high-resistance (HRS) and low-resistance (LRS) states were obtained after 100 repeated tests (Fig. 1d).

Biologically speaking, the different reactions of synapses to different external stimuli are considered to play a crucial part in information extraction [23]. Because the response of our device to voltage pulses is needed for realizing synaptic function [24], we investigated the conductance response to impulse voltages with different parameters (amplitude, interval, and width). Fig. 2a shows the conductance response of the device to pulses with fixed width (500 ns) and interval (500 ns) and varying amplitude (1–4 V in the positive range, and −1 to −4 V in the negative range). The device conductance obviously changed under the high-amplitude pulses but exhibited small changes under the low-amplitude pulses. The effects of varying pulse interval and width are presented in Fig. 2b, c, respectively (keeping the other two parameters constant in each case). Significant variations in the conductance were induced at longer durations and shorter intervals. These results clarify that the conductance of the designed device can be regulated by the voltage pulse, which is consistent with previous reports, thereby demonstrating the utility of memristors in neural morphological-information storage and processing systems [23,25,26].

The neurons in neuromorphic systems are connected through synapses, whose weights are adjusted to realize learning and memory. We clearly observed the potentiation/depression of synaptic weights under a pulse sequence of 20 set pulses and 20 reset pulses (Fig. 3a).
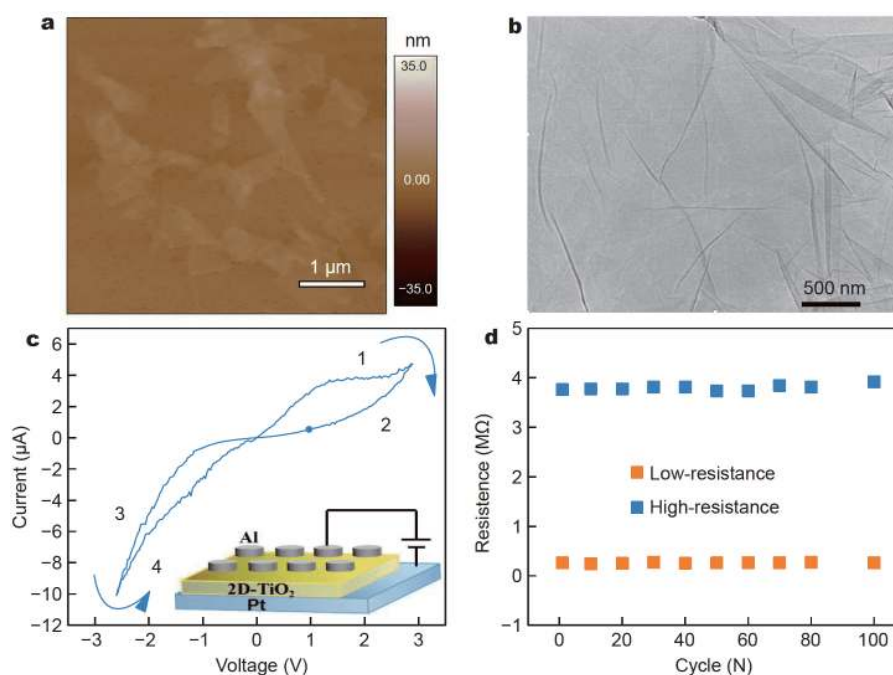
Figure 1 Structure and electrical performance of the fabricated memristor. (a) AFM image and (b) TEM image of the TiO_2 nanosheets. (c) I-V curve and structure of the device (inset). (d) Variations of maximum and minimum resistances obtained during a 100-iteration cycle test.
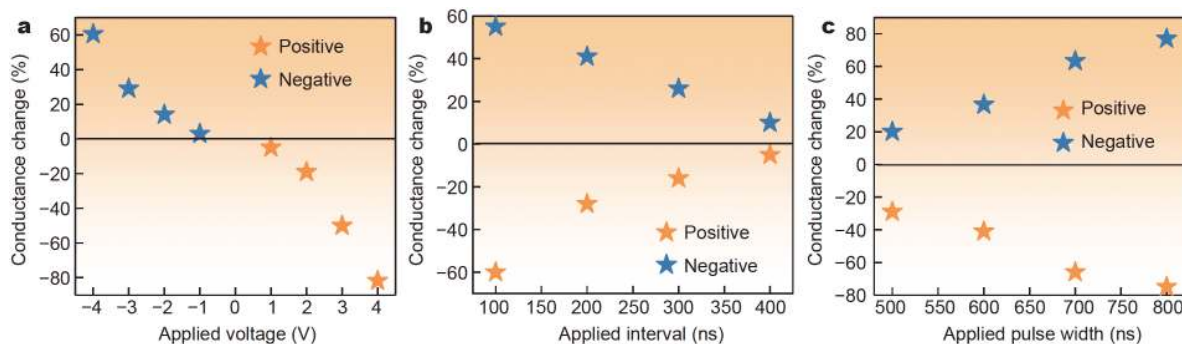
Figure 2 (a) Conductance change of the device under pulse voltage signals with different amplitudes, fixed width (500 ns), and fixed interval (500 ns). (b) Conductance change of the device under pulse voltage signals with different intervals, fixed amplitude ($\pm$ 2 V), and fixed width (500 ns). (c) Conductance change of the device under pulse voltage signals with different pulse widths, fixed amplitude ($\pm$ 2 V), and fixed interval (500 ns).

Combined with the I–V curve, we found that the conductance or resistance of the device can be regulated by electrical signals, similar to the change of synaptic weight. This proves that our device has the potential to simulate the synaptic function, learning, and memory behaviors [27–31]. The synapse consists of presynaptic membrane, synaptic space, and postsynaptic membrane. Here, the upper electrode Al is considered as presynaptic membrane, and the lower electrode Pt is considered as postsynaptic membrane (Fig. 3b). The applied voltage or pulse is used to simulate the electrical signals that are

transmitted between neurons, and the conductance changes are equivalent to the synaptic weight changes in real neurons. The results show that the device can successfully simulate typical synaptic plasticity: spike-timing-dependent plasticity (STDP) and paired-pulse facilitation (PPF). In biological synapses, the STDP explains the dependency between the synaptic weights and the time lag between the spike arrivals of the presynaptic and postsynaptic neurons [25]. Fig. S4 shows the pulse schemes for simulating STDP behavior, in which $\Delta t = t_{pre} - t_{post}$ is the time of spike stimulation at the postsynaptic mem-
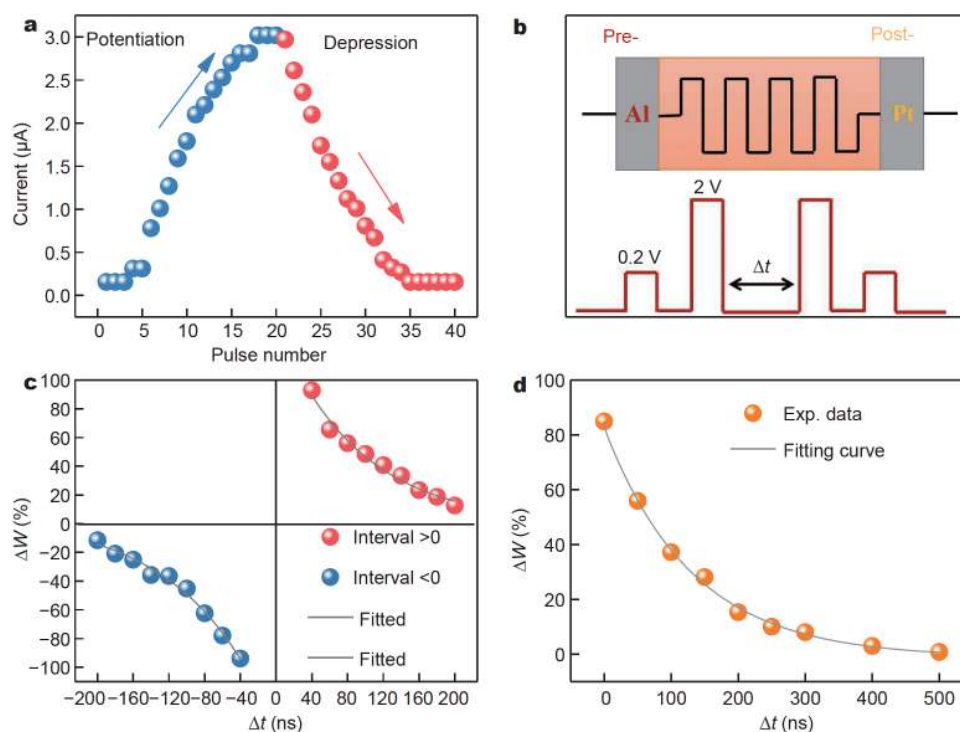
Figure 3 Basic synaptic plasticity. (a) The potentiation and depression characteristics of the synaptic weight exposed to a pulse train of 20 set pulses (amplitude = −2 V, interval = 500 ns, width = 500 ns) followed by 20 reset pulses (amplitude = 3 V, interval = 500 ns, width = 500 ns). (b) (Upper) synapse-like nature of the device structure and (lower) the pulse-waveform set for testing PPF. (c) STDP simulation results, showing the relationship between synaptic weight (ΔW) and Δt. (d) PPF characteristics of the device and their best-fit curve.

brane relative to that at the presynaptic membrane. Fig. 3c shows the experimental results of STDP. When $\Delta t > 0$ ($\Delta t < 0$), the presynaptic membrane received the spike stimulation earlier (later) than the postsynaptic membrane, so the synaptic weight increased (decreased) [32–34]. Moreover, the magnitude of the synaptic weight change ($\Delta W = (G_t - G_0)/G_0$) reduced with increasing Δt. Here, G_t and G_0 are the conductance extracted from the green and orange 0.2 V pulses in Fig. S4, respectively. The experimental results were fitted to the following equations:

$$\Delta W = A_+ \times e^{-t/\tau_+}, \quad \Delta t > 0, \tag{1}$$

$$\Delta W = A_- \times e^{-t/\tau_-}, \quad \Delta t < 0, \tag{2}$$

where A and τ refer to the scaling factor and time constant of the STDP . From the fitting results, A_+, A_-, τ_+, and τ_- were obtained as 1.38, −1.50, 92 ns, and −99 ns, respectively.

A typical short-term plasticity is PPF, which plays an important role in information transmission [35]. The PPF phenomenon refers to the strong dependence of the device response on the stimulation interval (Δt) between a pair of input stimuli. The synaptic weight gradually increases as the interval Δt decreases [36,37]. Under the pulse-waveform scheme shown at the bottom of Fig. 3b, the test results (Fig. 3d) were fitted to the equation of PPF = $(G_2 - G_1)/G_1 \times 100\%$ = $A_1\exp(-t/\tau_1) + A_2\exp(-t/\tau_2)$, where G_1 and G_2 are the conductance read from the front and rear low pulses, respectively [38]. The two fitting times τ_1 (1.22 ns) and τ_2 (131 ns) represent the fast and slow decaying items, respectively. Both STDP and PPF behaviors of our device are highly consistent with biological synapses.

Other typical synaptic phenomena are the long-term and short-term plasticities (LTP and STP, respectively), known as short-term memory (STM) and long-term memory (LTM) in the psychology literatures [23,39,40]. Biologically, STM holds the information that is quickly processed and encoded by the human brain; it persists for a few seconds to dozens of minutes. In contrast, LTM holds the information that is extensively and deeply processed; it persists for several days, weeks, or years. When held over one's lifetime, LTM is called permanent memory [37]. Repetitive stimulus triggers a transformation from STM to LTM [41]. Here, we verify the change in memory state by varying the numbers of pulses with

fixed amplitude (−2 V), width (500 ns), and interval (500 ns). After each pulse-train stimulation, the data maintenance (current change over time) was recorded at a reading voltage of 0.1 V. The results for different numbers of pulses are plotted in Fig. S5a–f. The synaptic weights were fitted using the following forgetting function [42]:

$$I_t = I_e + A \times e^{-t/\tau}. \tag{3}$$

Increasing the number of pulses increased both relaxation time τ and final stable weight I_e (Fig. S5g, h). To further prove that the memory state converts from STM to LTM, we read the maintained data half an hour after removing the stimulation (Fig. S5f). When fewer than 300 stimuli were applied, the synaptic weight decayed to zero. When the number of pulses exceeded 300, the memory lingered but the weight attenuated over time. These results strongly prove that the device's state converted from STM to LTM [43].

As mentioned above, the nociceptor is among the most important receptors in the body as it discriminates harmful stimuli and transmits pain signals to the central nervous system, thus avoiding potential damage [44–46]. In this study, we successfully reproduced the typical behavior of nociceptors by programming a memristor device with sensitization, desensitization, allodynia, and hyperalgesia. Table S1 is the benchmark table of nociceptor by memristor in recent research studies [31,47–50]. Sensitization, which facilitates avoidance of harmful stimulations, refers to the process of strengthening the reflex response. More specifically, a weak stimulus usually initiates a weak response but can initiate a much stronger response after an injurious stimulus [51]. For example, a human bitten by a snake will harbor a fear of snakes for ten years thereafter or longer. To reproduce this behavior, we designed the simulation scheme illustrated in Fig. 4a. The entire process was divided into three steps. We first applied a weak stimulus (Step 1), then a strong harmful stimulus (Step 2), and finally, a weak stimulus of the same magnitude as the first stimulus (Step 3). The interval between each step is 500 ns. The responses in each step were monitored for pulses with different amplitudes, pulse widths, and intervals to simulate external stimuli. Fig. 4b–d show the response currents at each step after exposure to high voltage (−2 V), small interval (100 ns), and long pulse width (500 ns), respectively. The response becomes larger after the strong stimulation (Step 2). In this process, the size of conductive filaments formed by oxygen vacancy increases gradually, which leads to a larger response under the same stimulus [28,52]. We then

changed the amplitude, interval, and pulse width of the strong simulation in Step 2; the results are plotted in Fig. 4e–g, respectively. Strengthening the stimulation in Step 2 enlarged the response current of the device and enhanced the degree of sensitization (Fig. 5a–c) [53]. Here, the pain sensitivity Y was defined as $Y = (A_1 - A_2)/A_1 \times 100\%$, where A_1 and A_2 are the current responses in Step 2 and Step 3 of the stimulus trains, respectively. The data of Fig. 5a–c were fitted to the following exponential equation:

$$Y = K_0 e^{A/A_0} + Y_0, \tag{4}$$

where K_0 and Y_0 are different sensitization constants, and A denotes an amplitude, a pulse width, or an interval. Note that varying the stimulus intensity A in Step 2 alters the pain sensitivity Y, consistent with the characteristics of biological sensitivity.

Further analyzing the responses before and after the strong stimulation (Fig. 4b–d, respectively), we found that the device mimicked the allodynia and hyperalgesia behaviors of real neurons (Fig. 5d–f). Allodynia means that the device is unresponsive to weak stimulation in the normal state but is responsive after injury. Hyperalgesia refers to the increased response to weak stimulation [17,49]. Corresponding to sensitivity is desensitization. We designed a pulse train to verify the desensitization (Fig. 6a), and the conductance difference (ΔG) of Step 3 and Step 1 is plotted in Fig. 6b. Increasing the time interval between Steps 2 and 3 decreased the ΔG, mimicking desensitization in the human nervous system, which may be due to the diffusion effect of oxygen vacancy with the increase of time interval [54,55].

To more quantitatively understand the effect of stimulus interval on desensitization, we fitted the experimental data to the following exponential equation (Fig. 6c):

$$Y = K_0 e^{-\Delta t/\tau} + Y_0, \tag{5}$$

where $Y = (G_3 - G_1)/G_1 \times 100\%$ is the sensitization degree (here, G_1 and G_3 are the response amplitudes of Step 1 and Step 3, respectively), Y_0 is the sensitization constant in the stable state, K_0 represents the sensitization factor, and τ is the relaxation time. It can be seen that the sensitivity gradually decreases with the increase of time interval and desensitization phenomenon enhanced [18].

Finally, we investigated the resistance switching mechanism of the system. We investigated that the conduction mechanism and temperature dependence of the HRS and LRS and found that the possible mechanism is electronic hopping between two sites rather than phase
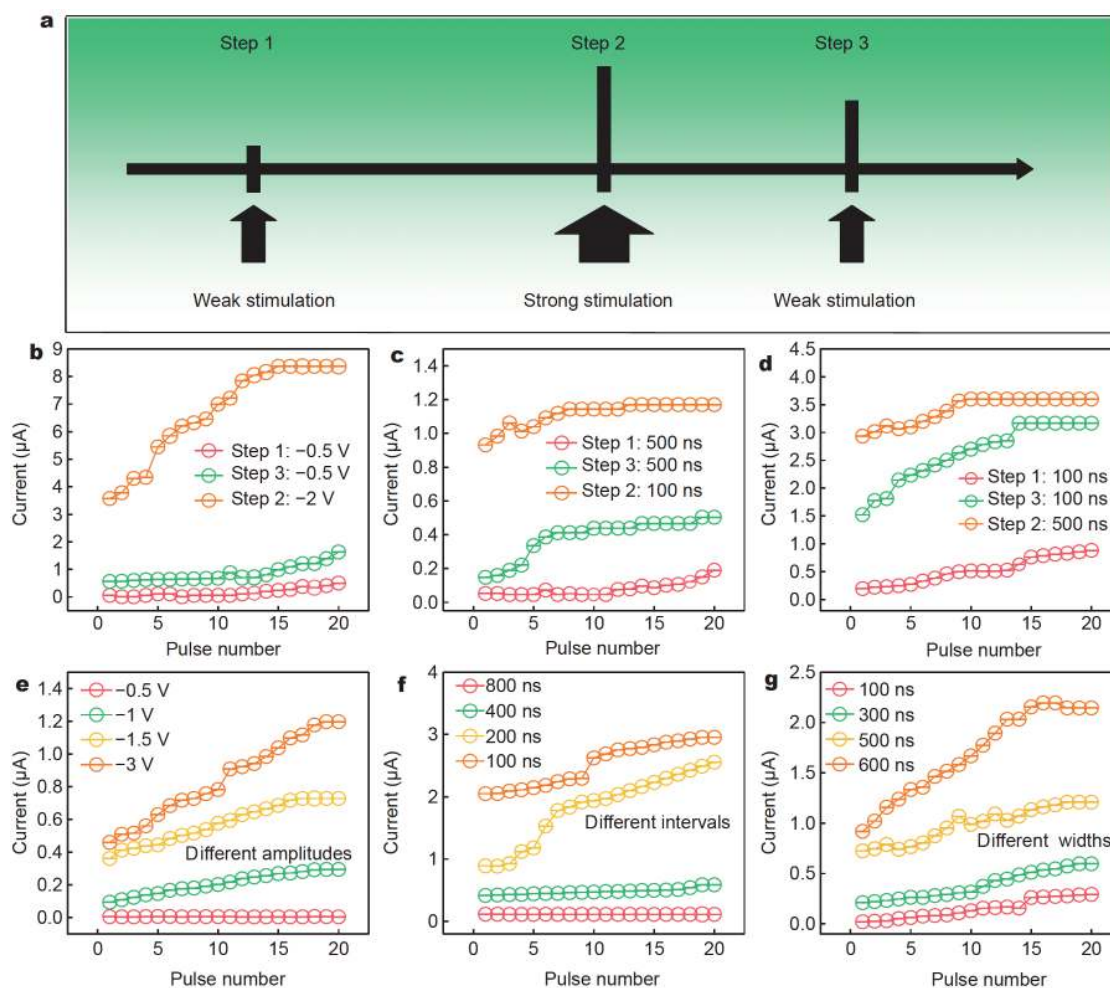
Figure 4 Mimicking the sensitization behavior of nociceptors. (a) Stimulus pattern for investigating sensitivity. Step 1 is a weak pulse stimulation (small amplitude, small pulse width, large interval), Step 2 is a strong pulse stimulation (large amplitude, large pulse width, small interval), and Step 3 repeats the weak stimulation of Step 1. (b–d) Sensitivity behaviors induced by pulses with large amplitude (−2 V), small interval (100 ns), and large width (500 ns), respectively. (e–g) Responses to different amplitudes, intervals, and widths of the stimulus pulse, respectively, in Step 2.

transition [56,57]. Hopping conduction can be expressed as follows:

$$J = qanv\exp\left[\frac{qaE}{kT} - \frac{W}{kT}\right], \tag{6}$$

where E is the strength of the electric field, q is the electronic charge, a is the distance between trap sites, n is the electron concentration in the conduction band of a dielectric, v is the thermal vibration frequency of the electrons at trap sites, T is the absolute temperature, k is Boltzmann's constant, and W is barrier height (activation energy). W and a are related as follows [58]:

$$W = W_m - \frac{e^2}{\pi\varepsilon\varepsilon_0 a}, \tag{7}$$

where W_m is the energy difference between the potential

wells of the localized states, ε is the dielectric constant of the matrix material and the band (or extended) state, ε_0 is the dielectric constant of vacuum, and e is the charge of an electron.

The I-V curves of the HRS and LRS at different temperatures were well fitted to the hopping conduction (see Fig. 7a, c). The trap spacing in TiO_2 was ~4.2 nm in the HRS and 3.3 nm in the LRS. According to the temperature dependence of curent density, the activation energy was ~0.6 eV in HRS and 0.1 eV in LRS, as shown in Fig. 7b, d, respectively, indicating the hopping of carrier got easier in the LRS and produced a large current [59]. We surmise that more oxygen vacancies were generated when the negative voltage increased, thus reducing the distance between the oxygen vacancies, lowering the ac-
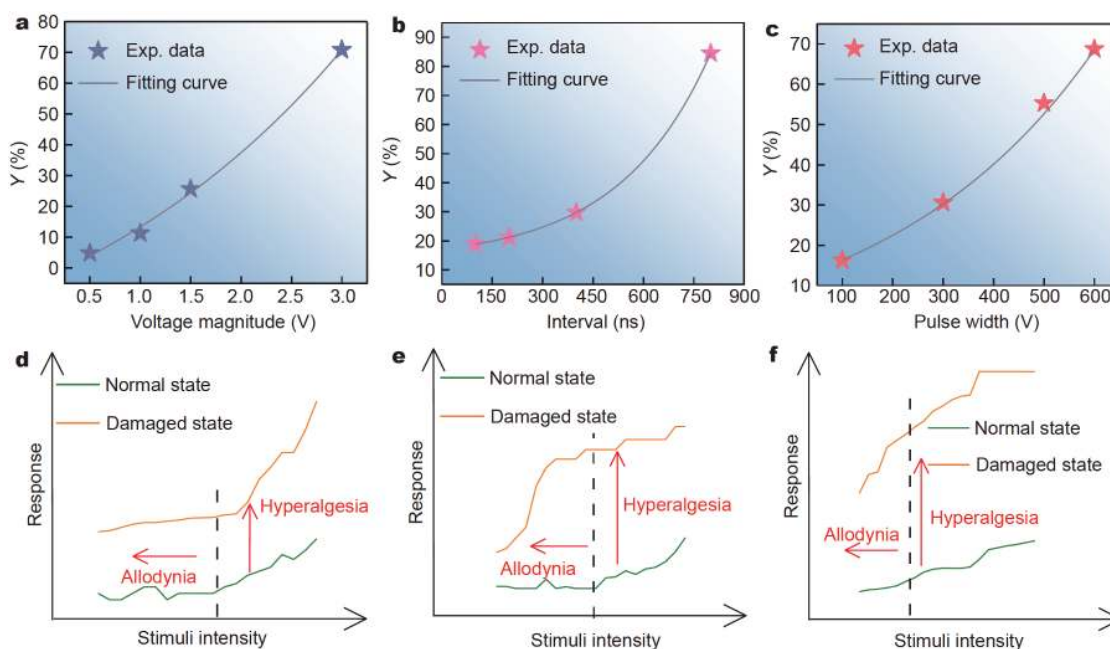
Figure 5 (a–c) Effects of stimulation intensity on the degree of pain sensitization. (d–f) Allodynia and hyperalgesia behaviors corresponding to Fig. 4b–d.
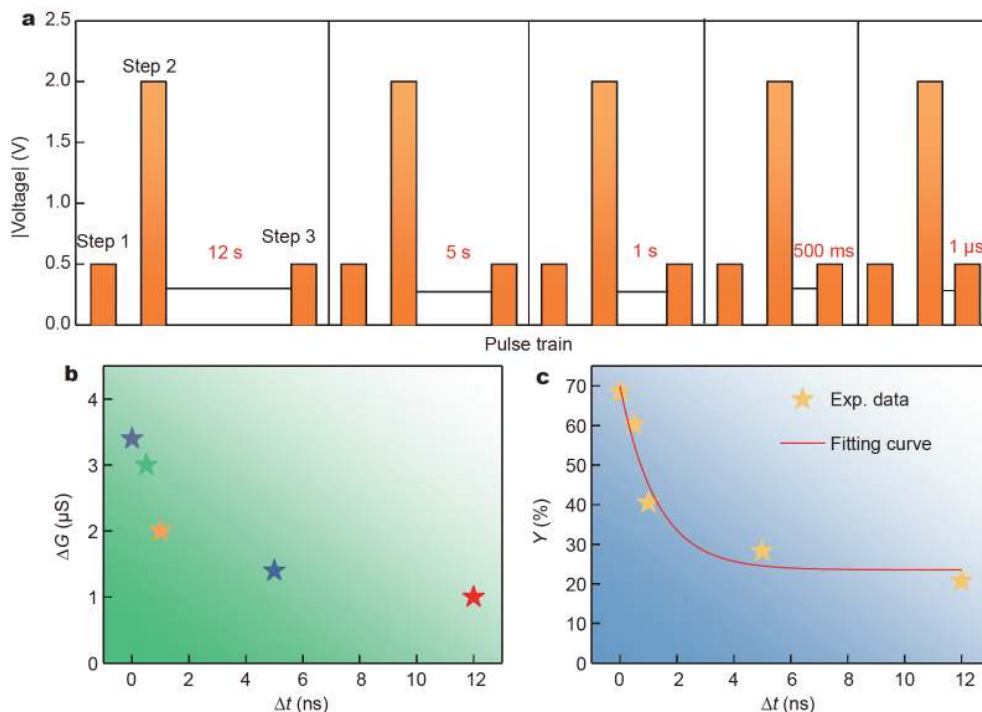
Figure 6 Mimicking the behavior of nociceptors: desensitization. (a) The desensitization phenomenon is verified by changing the time interval between Steps 2 and 3. (b) ΔG *versus* time interval (where Δt corresponds to (a)). (c) The Y index plotted as a function of the time interval between Steps 2 and 3.
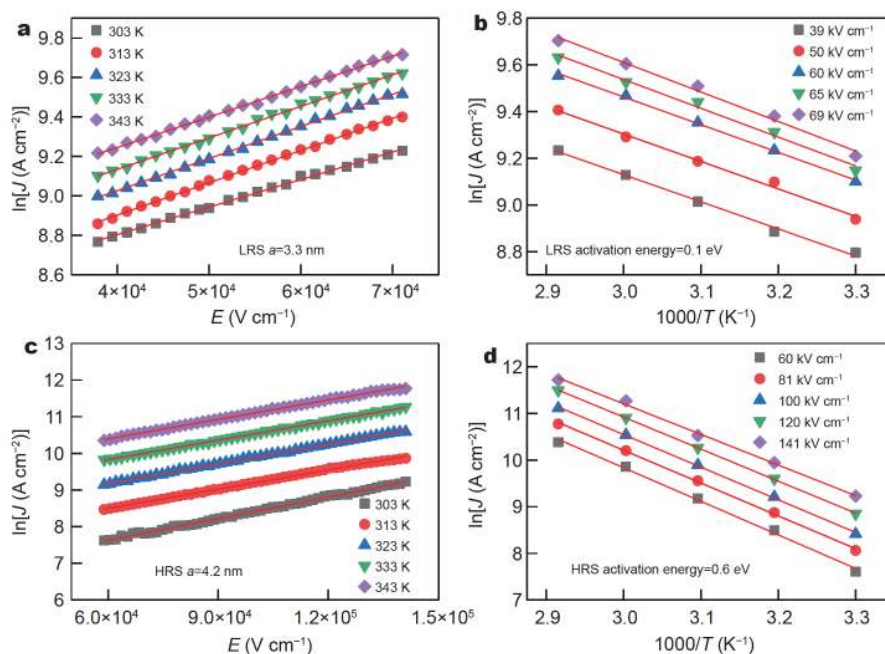
Figure 7 (a) ln$J$–E curves of LRS. The trap spacing is 3.3 nm. (b) The temperature dependence of current density of LRS segments. The activation energy is 0.1 eV. (c) ln$J$–E curves of HRS. The trap spacing is 4.2 nm. (d) The temperature dependence of current density of HRS segments. The activation energy is 0.6 eV.

tivation energy, and facilitating carrier jump. Accordingly, the device switched from HRS to LRS [60]. Fig. S6 illustrates this mechanism in detail.

CONCLUSION

We prepared an Al/TiO$_2$/Pt memristor *via* a simple spin coating method and demonstrated its advantageous and stable electrical properties. The conductance of the device was modulated by a pulse voltage, and biological synapse behaviors such as STDP and PPF were successfully simulated. We also analyzed the *I-V* curve of the device. The HRS and LRS follow a hopping conduction mechanism. Most importantly, we proposed and validated a new method for reproducing the behavior of nociceptors, including sensitization, desensitization, allodynia, and hyperalgesia. These novel biomimetic functions might expand the application of TiO$_2$ to electronic skins, humanoid robots, and similar technologies, and will aid the establishment of hardware-based neural morphological networks in the future.

1. Seok Jeong D, Kim I, Ziegler M, *et al.* Towards artificial neurons and synapses: A materials point of view. RSC Adv, 2013, 3: 3169–3183

2. Jo SH, Chang T, Ebong I, *et al.* Nanoscale memristor device as synapse in neuromorphic systems. Nano Lett, 2010, 10: 1297–1301

3. Yan X, Zhao Q, Chen A, *et al.* Vacancy-induced synaptic behavior in 2D WS$_2$ nanosheet-based memristor for low-power neuromorphic computing. Small, 2019, 15: 1901423

4. Tan H, Liu G, Zhu X, *et al.* An optoelectronic resistive switching memory with integrated demodulating and arithmetic functions. Adv Mater, 2015, 27: 2797–2803

5. Boyn S, Grollier J, Lecerf G, *et al.* Learning through ferroelectric domain dynamics in solid-state synapses. Nat Commun, 2017, 8: 14736

6. Chandrasekaran S, Simanjuntak FM, Saminathan R, *et al.* Improving linearity by introducing Al in HfO$_2$ as a memristor synapse device. Nanotechnology, 2019, 30: 445205

7. Zhao Q, Xie Z, Peng YP, *et al.* Current status and prospects of memristors based on novel 2D materials. Mater Horiz, 2020, 7: 1495–1518

8. Yuan J, Lou J. Memristor goes two-dimensional. Nat Nanotech, 2015, 10: 389–390

9. Yang Y, Du H, Xue Q, *et al.* Three-terminal memtransistors based on two-dimensional layered gallium selenide nanosheets for potential low-power electronics applications. Nano Energy, 2019, 57: 566–573

10. Ge R, Wu X, Kim M, *et al.* Atomristor: Nonvolatile resistance switching in atomic sheets of transition metal dichalcogenides. Nano Lett, 2018, 18: 434–441

11. Wang M, Cai S, Pan C, *et al.* Robust memristors based on layered two-dimensional materials. Nat Electron, 2018, 1: 130–136

12. Li D, Wu B, Zhu X, *et al.* MoS$_2$ memristors exhibiting variable switching characteristics toward biorealistic synaptic emulation. ACS Nano, 2018, 12: 9240–9252

13 Senthilkumar V, Kathalingam A, Kannan V, *et al.* Observation of multi-conductance state in solution processed Al/a-TiO$_2$/ITO memory device. Microelectron Eng, 2012, 98: 97–101

14 Son D, Lee J, Qiao S, *et al.* Multifunctional wearable devices for diagnosis and therapy of movement disorders. Nat Nanotech, 2014, 9: 397–404

15 Jo A, Seo Y, Ko M, *et al.* Textile resistance switching memory for fabric electronics. Adv Funct Mater, 2017, 27: 1605593

16 Gold MS, Gebhart GF. Nociceptor sensitization in pain pathogenesis. Nat Med, 2010, 16: 1248–1257

17 Yoon JH, Wang Z, Kim KM, *et al.* An artificial nociceptor based on a diffusive memristor. Nat Commun, 2018, 9: 417

18 Feng G, Jiang J, Zhao Y, *et al.* A sub-10 nm vertical organic/inorganic hybrid transistor for pain-perceptual and sensitization-regulated nociceptor emulation. Adv Mater, 2020, 32: 1906171

19 Hou J, Zheng Y, Su Y, *et al.* Macroscopic and strong ribbons of functionality-rich metal oxides from highly ordered assembly of unilamellar sheets. J Am Chem Soc, 2015, 137: 13200–13208

20 Srivastava S, Thomas JP, Leung KT. Programmable, electroforming-free TiO$_x$/TaO$_x$ heterojunction-based non-volatile memory devices. Nanoscale, 2019, 11: 18159–18168

21 Edwards AH, Barnaby HJ, Campbell KA, *et al.* Reconfigurable memristive device technologies. Proc IEEE, 2015, 103: 1004–1033

22 Tang Z, Chi Y, Fang L, *et al.* Resistive switching effect in titanium oxides. J Nanosci Nanotech, 2014, 14: 1494–1507

23 Yang M, Zhao X, Tang Q, *et al.* Stretchable and conformable synapse memristors for wearable and implantable electronics. Nanoscale, 2018, 10: 18135–18144

24 Li Y, Zhong Y, Zhang J, *et al.* Activity-dependent synaptic plasticity of a chalcogenide electronic synapse for neuromorphic systems. Sci Rep, 2015, 4: 4906

25 Tan ZH, Yin XB, Yang R, *et al.* Pavlovian conditioning demonstrated with neuromorphic memristive devices. Sci Rep, 2017, 7: 713

26 Yan X, Zhang L, Chen H, *et al.* Graphene oxide quantum dots based memristors with progressive conduction tuning for artificial synaptic learning. Adv Funct Mater, 2018, 28: 1803728

27 Park Y, Lee JS. Artificial synapses with short- and long-term memory for spiking neural networks based on renewable materials. ACS Nano, 2017, 11: 8962–8969

28 Wang C, He W, Tong Y, *et al.* Investigation and manipulation of different analog behaviors of memristor as electronic synapse for neuromorphic applications. Sci Rep, 2016, 6: 22970

29 Zhou Z, Zhao J, Chen AP, *et al.* Designing carbon conductive filament memristor devices for memory and electronic synapse applications. Mater Horiz, 2020, 7: 1106–1114

30 Xing Y, Shi C, Zhao J, *et al.* Mesoscopic-functionalization of silk fibroin with gold nanoclusters mediated by keratin and bioinspired silk synapse. Small, 2017, 13: 1702390

31 Yang X, Fang Y, Yu Z, *et al.* Nonassociative learning implementation by a single memristor-based multi-terminal synaptic device. Nanoscale, 2016, 8: 18897–18904

32 Zhao J, Zhou Z, Zhang Y, *et al.* An electronic synapse memristor device with conductance linearity using quantized conduction for neuroinspired computing. J Mater Chem C, 2019, 7: 1298–1306

33 Wang G, Yan X, Chen J, *et al.* Memristors based on the hybrid structure of oxide and boron nitride nanosheets combining memristive and neuromorphic functionalities. Phys Status Solidi RRL, 2020, 14: 1900539

34 Yan X, Qin C, Lu C, *et al.* Robust Ag/ZrO$_2$/WS$_2$/Pt memristor for

35 neuromorphic computing. ACS Appl Mater Interfaces, 2019, 11: 48029–48038

35 Abbott LF, Regehr WG. Synaptic computation. Nature, 2004, 431: 796–803

36 Yan X, Pei Y, Chen H, *et al.* Self-assembled networked PbS distribution quantum dots for resistive switching and artificial synapse performance boost of memristors. Adv Mater, 2019, 31: 1805284

37 Chang T, Jo SH, Lu W. Short-term memory to long-term memory transition in a nanoscale memristor. ACS Nano, 2011, 5: 7669–7676

38 Pei Y, Zhou Z, Chen AP, *et al.* A carbon-based memristor design for associative learning activities and neuromorphic computing. Nanoscale, 2020, 12: 13531–13539

39 Ohno T, Hasegawa T, Tsuruoka T, *et al.* Short-term plasticity and long-term potentiation mimicked in single inorganic synapses. Nat Mater, 2011, 10: 591–595

40 Hwang H–, Woo J–, Lee T–, *et al.* Synaptic plasticity and preliminary-spike-enhanced plasticity in a CMOS-compatible Ta$_2$O$_5$ memristor. Mater Des, 2020, 187: 108400

41 Jiang R, Ma P, Han Z, *et al.* Habituation/fatigue behavior of a synapse memristor based on IGZO-HfO$_2$ thin film. Sci Rep, 2017, 7: 9354

42 Sokolov AS, Ali M, Riaz R, *et al.* Silver-adapted diffusive memristor based on organic nitrogen-doped graphene oxide quantum dots (N-GOQDs) for artificial biosynapse applications. Adv Funct Mater, 2019, 29: 1807504

43 Qu B, Du H, Wan T, *et al.* Synaptic plasticity and learning behavior in transparent tungsten oxide-based memristors. Mater Des, 2017, 129: 173–179

44 Kumar M, Kim HS, Kim J. A highly transparent artificial photonic nociceptor. Adv Mater, 2019, 31: 1900021

45 Basbaum AI, Bautista DM, Scherrer G, *et al.* Cellular and molecular mechanisms of pain. Cell, 2009, 139: 267–284

46 Dubin AE, Patapoutian A. Nociceptors: The sensors of the pain pathway. J Clin Invest, 2010, 120: 3760–3772

47 Xiao M, Shen D, Futscher MH, *et al.* Threshold switching in single metal-oxide nanobelt devices emulating an artificial nociceptor. Adv Electron Mater, 2020, 6: 1900595

48 Dev D, Shawkat MS, Krishnaprasad A, *et al.* Artificial nociceptor using 2D MoS$_2$ threshold switching memristor. IEEE Electron Device Lett, 2020, 41: 1440–1443

49 Ge J, Zhang S, Liu Z, *et al.* Flexible artificial nociceptor using a biopolymer-based forming-free memristor. Nanoscale, 2019, 11: 6591–6601

50 Kim Y, Kwon YJ, Kwon DE, *et al.* Nociceptive memristor. Adv Mater, 2018, 30: 1704320

51 Wang L, Wang Z, Lin J, *et al.* Long-term homeostatic properties complementary to Hebbian rules in CuPc-based multifunctional memristor. Sci Rep, 2016, 6: 35273

52 Simanjuntak FM, Chandrasekaran S, Lin CC, *et al.* ZnO$_2$/ZnO bilayer switching film for making fully transparent analog memristor devices. APL Mater, 2019, 7: 051108

53 Zhao B, Xiao M, Shen D, *et al.* Heterogeneous stimuli induced nonassociative learning behavior in ZnO nanowire memristor. Nanotechnology, 2020, 31: 125201

54 Yu S, Wong HSP. A phenomenological model for the reset mechanism of metal oxide RRAM. IEEE Electron Device Lett, 2010, 31: 1455–1457

55 Sarkar B, Lee B, Misra V. Understanding the gradual reset in Pt/

Al₂O₃/Ni RRAM for synaptic applications. Semicond Sci Technol, 2015, 30: 105014

56 Yan XB, Hao H, Chen YF, et al. Highly transparent bipolar resistive switching memory with In-Ga-Zn-O semiconducting electrode in In-Ga-Zn-O/Ga₂O₃/In-Ga-Zn-O structure. Appl Phys Lett, 2014, 105: 093502

57 Manna A, Barman A, Joshi SR, et al. The effect of Ti⁺ ion implantation on the anatase-rutile phase transformation and resistive switching properties of TiO₂ thin films. J Appl Phys, 2018, 124: 155303

58 Pike GE. Ac conductivity of scandium oxide and a new hopping model for conductivity. Phys Rev B, 1972, 6: 1572–1580

59 Chang YF, Fowler B, Chen YC, et al. Intrinsic SiOₓ-based unipolar resistive switching memory. II. Thermal effects on charge transport and characterization of multilevel programing. J Appl Phys, 2014, 116: 043709

60 Park JW, Park JW, Kim DY, et al. Reproducible resistive switching in nonstoichiometric nickel oxide films grown by RF reactive sputtering for resistive random access memory applications. J Vacuum Sci Tech A-Vacuum Surfs Films, 2005, 23: 1309–1313

Author contributions Yan X proposed the idea of this research and revised the paper; Lan J completed the performance test of the device and prepared the manuscript; Cao G and Wang J coordinated the work. All authors contributed to the general discussion.

Conflict of interest The authors declare that they have no conflict of interest.

Supplementary information Supporting data are available in the online version of this paper.

Jinling Lan received her BSc degree in electronic information science and technology from the School of Information Technology, Hebei Normal University in 2018. She is currently a ME student of Hebei University. Her current research focuses on the field of memristors.

Gang Cao received his BSc degree in electronic information science and technology from the School of Electronic Information and Physics of Changzhi College in 2018. He is now a student of Hebei University. His current research focuses on the field of memristors.

Jingjuan Wang received her BSc degree in communication engineering from the Department of Electronic Information Engineering, Tangshan University, China, in 2016. She is currently a DE student at Hebei University. Her current research focuses on the field of memristors.

Xiaobing Yan is currently a professor at the School of Electronic and Information Engineering, Hebei University. He received his PhD degree from Nanjing University in 2011. From 2014 to 2016, he held the research fellow position at the National University of Singapore. His current research focuses on the field of memristors.

一种基于TiO₂纳米片忆阻器的人工伤害感受器

兰晋玲[1†], 曹刚[1], 王静娟[1], 闫小兵[1,2†*]

摘要 人工忆阻突触的学习记忆功能是实现人工神经网络和神经形态计算的必要条件. 纳米片材料由于其良好的可扩展性, 在细胞级学习水平中得到了广泛的应用, 但基于纳米片材料的伤害感受器行为研究却鲜有报道. 本文中, 我们提出了一种具有Al/TiO₂/Pt结构的忆阻器. 电铸后, 忆阻器呈现出逐渐的电导调节, 并能模拟突触功能, 如突触重量的增加和降低. 我们还设计了一个新的方案来验证真实伤害感受器的痛觉敏感、脱敏、超敏和痛觉过敏行为. 具有这些特性的忆阻器可以显著提高智能电子器件的性能. 数据拟合表明, 高阻和低阻状态符合跳跃导电机制. 这项工作使得基于TiO₂的器件有望应用于下一代神经形态学系统.